

Vector-total field magnetometry and calibration using NV center ensembles

Kai-Hui Wang(王凯辉), Yun-Bin Zhu(朱云彬), Zi-Yun Yu(于子云), Xiang Li(李想), Xiang-Mei Xu(许祥妹), Zhao Zhao(赵昭), Liang Zhang(张亮), Ke Jing(靖克), and Yi-Jin Xie(谢一进)

Citation: Chin. Phys. B, 2026, 35 (**7**): 070706. DOI: 10.1088/1674-1056/ae12d5
http://cpb.iphy.ac.cn; http://iopscience.iop.org/cpb

What follows is a list of articles you may be interested in

Spin-based magnetic detection of optically trapped single cell in microfluidic channel

Jun Yin(殷俊), Sanyou Chen(陈三友), Yihao Yan(燕一皓), Mengqi Wang(王孟祺), Ya Wang(王亚), Yiheng Lin(林毅恒), Qi Zhang(张琪), and Fazhan Shi(石发展)

Chin. Phys. B, 2025, 34 (**7**): 070704. DOI: 10.1088/1674-1056/adde38

Vector magnetometry in zero bias magnetic field using nitrogen-vacancy ensembles

Chunxing Li(李春兴), Fa-Zhan Shi(石发展), Jingwei Zhou(周经纬), and Peng-Fei Wang(王鹏飞)

Chin. Phys. B, 2024, 33 (**10**): 100701. DOI: 10.1088/1674-1056/ad73af

A robust method for performance evaluation of the vapor cell for magnetometry

Zhi Liu(柳治), Sheng Zou(邹升), Kaifeng Yin(尹凯峰), Tao Shi(石韬),Junjian Tang(唐钧剑), and Heng Yuan(袁珩)

Chin. Phys. B, 2023, 32 (**4**): 040703. DOI: 10.1088/1674-1056/aca6d5

Indirect pumping bell-bloom magnetometer

Meng-Bing Wang(王梦冰), Da-Fa Zhao(赵大法), Gui-Ying Zhang(张桂迎), Kai-Feng Zhao(赵凯锋)

Chin. Phys. B, 2017, 26 (**10**): 100701. DOI: 10.1088/1674-1056/26/10/100701

Spin dynamics of magnetic resonance with parametric modulation in a potassium vapor cell

Rui Zhang(张锐), Zhi-Guo Wang(汪之国), Xiang Peng(彭翔), Wen-Hao Li(黎文浩), Song-Jian Li(李松健), Hong Guo(郭弘)

Chin. Phys. B, 2017, 26 (**3**): 030701. DOI: 10.1088/1674-1056/26/3/030701

Vector-total field magnetometry and calibration using NV center ensembles

Kai-Hui Wang(王凯辉)[1,2,3,4,†], Yun-Bin Zhu(朱云彬)[1,3,4,†], Zi-Yun Yu(于子云)[5,6], Xiang Li(李想)[7], Xiang-Mei Xu(许祥妹)[7], Zhao Zhao(赵昭)[2,‡], Liang Zhang(张亮)[1,3,4], Ke Jing(靖克)[5,6,§], and Yi-Jin Xie(谢一进)[1,3,4,¶]

[1] *Institute of Quantum Sensing and School of Physics, Zhejiang University, Hangzhou* 310027, *China*
[2] *Donghai Laboratory, Zhoushan* 316000, *China*
[3] *Institute of Fundamental and Transdisciplinary Research and State Key Laboratory of Ocean Sensing, Zhejiang University, Hangzhou* 310058, *China*
[4] *Zhejiang Key Laboratory of Research and Development and Application of Cutting-edge Scientific Instruments, Zhejiang University, Hangzhou* 310058, *China*
[5] *CAS (Chinese Academy of Sciences) Key Laboratory of Microscale Magnetic Resonance and School of Physical Sciences, University of Science and Technology of China, Hefei* 230026, *China*
[6] *Anhui Province Key Laboratory of Scientific Instrument Development and Application, University of Science and Technology of China, Hefei* 230026, *China*
[7] *Jianghuai Advance Technology Center, Hefei* 230000, *China*

(Received 27 July 2025; revised manuscript received 25 September 2025; accepted manuscript online 14 October 2025)

Given the limitations in payload capacity and power availability on spacecraft, magnetometers capable of measuring both the vector and total magnetic fields are especially valuable for their compact and versatile design. Nitrogen-vacancy (NV) center ensembles offer precise vector magnetic field measurement capabilities, making them promising candidates for spaceborne magnetic sensing technologies. Here, we develop a technique to validate the vector–total field measurement accuracy performed by NV center ensembles. The validation procedure employs a turntable to simultaneously calibrate the bias magnetic field and quantify the uncertainty associated with total magnetic field measurements. Validation tests conducted in a geomagnetic field environment reveal a measured standard deviation of 0.1 μT, which is 0.2% relative to the geomagnetic field. With further refinement, the accuracy of total magnetic field measurements may improve to better than 0.01%. These results provide a valuable reference for the further development of vector–total field magnetometers and hold potential for applications in spacecraft.

Keywords: magnetometry, nitrogen-vacancy ensembles, vector-total field

PACS: 07.55.Ge, 76.30.Mi, 76.70.Hb, 42.50.Dv

DOI: 10.1088/1674-1056/ae12d5 **CSTR:** 32038.14.CPB.ae12d5

1. Introduction

Magnetometers are widely incorporated into spacecraft, supporting essential functions such as attitude determination[1] and navigation.[2,3] In particular, research satellites utilize them to investigate variations in the geomagnetic field[4] and to monitor solar activity.[5] For such applications, accurate magnetic field measurements are critical to ensuring reliable aerospace detection and analysis. Over the years, vector fluxgate magnetometers[6] have remained the preferred choice for satellites due to their low power consumption, lightweight design, and exceptional reliability.[7] By employing a three-component system, vector magnetometers can reconstruct the complete information of the field. However, inconsistencies such as offset errors, scaling factor discrepancies and assembly misalignments among the three axes inevitably result in measurement inaccuracies.[8] To address these, scalar atomic magnetometers[9,10] are often deployed as secondary instruments to support the calibration of vector magnetometers.[7,8,11,12]

Magnetometers based on nitrogen-vacancy (NV) centers promise to define the next generation of satellite magnetic sensors.[13] Compared to traditional vector magnetometers, the intrinsic lattice structure of diamond provides NV center ensembles with exceptional stability and uniformity as probes for vector magnetic fields.[14] This inherent crystallographic coordinate system also facilitates precise reconstruction of the total magnetic field, eliminating the need for additional calibration. Furthermore, their atomic-scale dimensions and long coherence times at room temperature[15] enable them to function as sensitive magnetic probes with nanoscale resolution.[16,17] Crucially, the entire probe is compatible with

† These authors contributed equally to this work.
‡Corresponding author. E-mail: zhaozhao@donghailab.com
§Corresponding author. E-mail: jk1994@ustc.edu.cn
¶Corresponding author. E-mail: xie1jin@zju.edu.cn

© 2026 Chinese Physical Society and IOP Publishing Ltd. All rights, including for text and data mining, AI training, and similar technologies, are reserved.

compact CMOS integration,[18] significantly reducing spatial and weight constraints.

In this work, we employ the ground-state Hamiltonian of the NV center to extract the absolute vector magnetic field, and introduce a technique for quantifying the uncertainty associated with total magnetic field measurements, alongside simultaneous calibration of the bias field. By rotating the magnetometer probe and sampling the magnetic field in different orientations, we obtain a set of vector measurements that are subsequently fitted to a sphere in three-dimensional space. The center of the fitted sphere corresponds to the bias magnetic field. Vectorial subtraction of the bias field from each measurement yields the true magnetic field. Subject to environmental disturbances, the reconstruction of the total magnetic field exhibits a deviation of 0.2%. This approach enables more compact spacecraft sensor architectures and facilitates higher-precision magnetic field characterization.

2. Materials and methods

The NV center is a defect in the diamond lattice that occurs when a nitrogen atom substitutes for a carbon atom, accompanied by a vacancy at an adjacent lattice site. In diamond, NV centers are oriented along four distinct crystallographic directions, as illustrated in Fig. 1(a). The NV center can exist in an electrically neutral state or possess either a single positive or negative charge.[19] Among these, NV^- centers are preferentially utilized for quantum sensing due to their unique properties.[20] This configuration involves an additional electron being captured at the vacancy site, resulting in a spin $S=1$ system. The ground state of the NV^- center is a spin triplet state, $^3A_2$, in which the energy of the $|m_s=0\rangle$ state is separated from that of the $|m_s=\pm1\rangle$ states by a zero-field splitting D_{gs}, as illustrated in Fig. 1(b). An external magnetic field $\boldsymbol{B_0}=(B_x,B_y,B_z)$ lifts the degeneracy of the $|m_s=\pm1\rangle$ states via the Zeeman effect. The electron-spin Hamiltonian for each of the four NV orientations $i=1,2,3,4$ in the ground state can be approximated as[21]

$$H^i/h=\left(D_{gs}+M^i_{z_i}\right)(S^i_{z_i})^2+\gamma\boldsymbol{B_0}\cdot\boldsymbol{S^i}+M_{x_i}(S^2_{y_i}-S^2_{x_i})+M_{y_i}(S_{x_i}S_{y_i}+S_{y_i}S_{x_i}). \quad (1)$$

Here D_{gs} is the zero-field splitting parameter, which is approximately 2.87 GHz at room temperature.[14] $\gamma\approx28.03$ GHz/T is the gyromagnetic ratio of the NV center.[22] $\boldsymbol{S^i}=(S^i_{x_i},S^i_{y_i},S^i_{z_i})$ is the electronic spin-1 operator. $(M^i_{x_i},M^i_{y_i},M^i_{z_i})$ are the spin–strain coupling parameters along x_i-, y_i-, z_i-directions. The set (x_i,y_i,z_i) defines the Cartesian coordinate axes of NV centers with orientation i, where z_i is aligned with the principal axis of NV center structure.

NV centers in the ground state $^3A_2$ can be optically pumped to the excited state ^3E using a 520-nm laser. The subsequent decay process is spin-selective.[23,24] Under continuous laser irradiation, the NV ensembles become polarized into the $|m_s=0\rangle$ spin sublevel of the ground state after several excitation-decay cycles.[24] Population distribution among the ground-state sublevels can be manipulated by applying microwaves (MW).[25] In the continuous-wave optically detected magnetic resonance (cw-ODMR) method, the resonant frequencies are extracted from the ODMR spectrum.[14] The vector magnetic field $\boldsymbol{B_0}$ is reconstructed by inverting the measured frequencies using the Levenberg–Marquardt algorithm, according to Eq. (1). Since the system is under-constrained, the spin–strain coupling parameters $(M^i_{y_i},M^i_{z_i})$ are set to zero throughout the calculation.

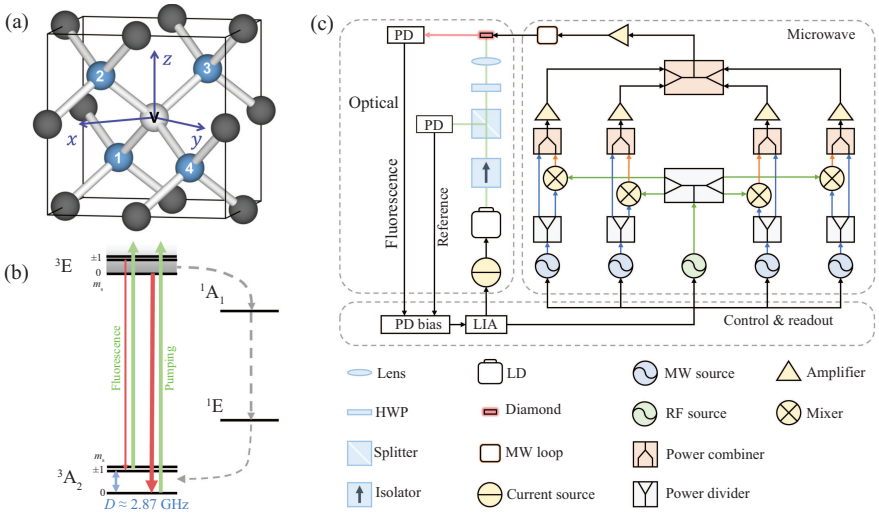


Fig. 1. (a) Four crystallographic orientations of NV centers in diamond. "V" represents a vacancy in the diamond lattice, while a nitrogen atom is situated in one of four adjacent positions, which are labeled by 1–4. (b) Energy level structure of NV center. A 520-nm pump laser excites the ground state $^3A_2$ to excited state ^3E. The excited NV centers either directly return to the ground state, emitting red fluorescence, or undergo a non-radiative transition via the two intermediate states $^1A_1$ and ^1E. (c) Schematic diagram of the sensor. A 520-nm laser beam is generated by a laser diode (LD) and split into two paths. One is focused onto the diamond sample, while the other is directly collected by a photodiode (PD) and utilized for noise cancellation via destructive interference. A microwave source, controlled by a lock-in amplifier (LIA), manipulates the spin states of NV centers. The resulting fluorescence is converted to a digital signal and recorded by the lock-in amplifier.

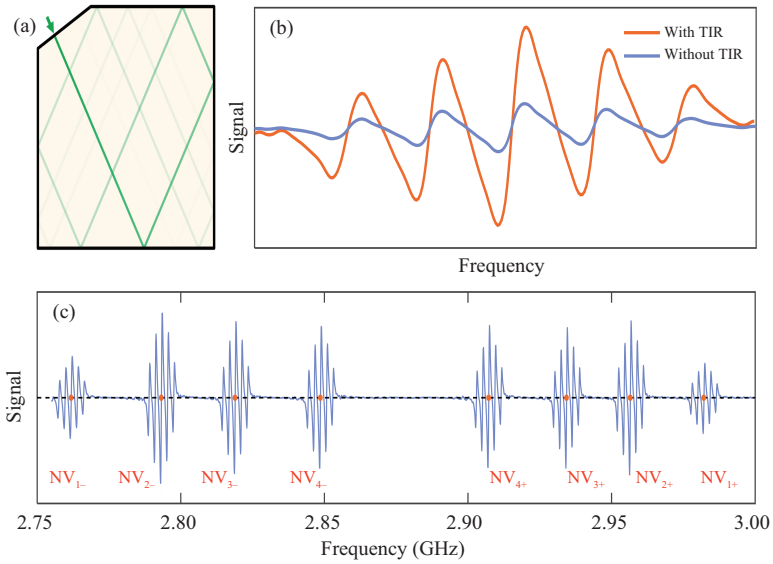


Fig. 2. (a) Total internal reflection (TIR) in diamond sample. (b) Comparison of signal intensity under TIR and non-TIR conditions. (c) The ODMR spectrum. The resonant frequencies are identified from the zero-crossing points of the frequency-modulated MW signal.

The overall system configuration of the magnetometer is illustrated in Fig. 1(c). It achieves a total magnetic field sensitivity of 2.5 nT/Hz$^{1/2}$.[26,27] The sensor probe is a square, thin-plate diamond sample with an angled cutout, as depicted in Fig. 2(a). A 520-nm laser beam is directed through the cut face, which undergoes total internal reflection within the sample,[28] significantly improving the laser utilization efficiency, as shown in Fig. 2(b). The laser polarization is finely tuned using a half-wave plate to optimally excite all four orientations of NV centers.[29] The MW module is specially designed to manipulate the spin state of NV centers. It consists of four channels, each generating MW signals with distinct frequencies to scan specific ranges around the resonant frequencies, which are separated by the applied bias magnetic field.[14] In the cw-ODMR method, the laser remains continuously on, and the fluorescence intensity drops at MW resonances. To simultaneously read out four resonant frequencies while improving the probe's sensitivity, MW signals are frequency modulated,[30] amplified and then delivered to the diamond sample. The emitted red fluorescence of NV centers is detected by a PD and subsequently processed through a PD bias circuit to optimize signal-to-noise ratio. Finally, the resulting digital signal is demodulated by a home-built LIA to extract four resonant frequencies corresponding to four NV center orientations. Given that eight resonant frequencies are involved, two scanning iterations are required to obtain the complete ODMR spectrum, as demonstrated in Fig. 2(c). Within each scanned frequency range, the frequency at the central zero-crossing point (the red point in Fig. 2(c)) is selected to compute the vector magnetic field via the Levenberg–Marquardt algorithm.

The resultant measurement is a superposition of the environmental magnetic field and the bias magnetic field. To isolate the latter, the probe is mounted on a turntable that allows it to rotate within a plane. Figure 3(a) illustrates the experimental process, where the rotating turntable allows the probe to record the vector magnetic field at different angles in a single plane. In the experiments, the cw-ODMR method is employed at each 30° rotation interval to acquire the eight resonant frequencies and compute the corresponding vector magnetic field. The set of vector measurements forms a circular distribution in three-dimensional (3D) space. By adjusting the probe's orientation relative to the turntable, the data points instead trace out a sphere,[12] whose center corresponds to the vector of the bias magnetic field. Consequently, both the bias field and the deviation of the total environmental field can be resolved through spherical fitting of measurements acquired at varied probe orientations.

3. Results and discussion

Total geomagnetic field measurements were performed in an environment with minimal magnetic perturbations that were maintained below 1 nT. The environmental magnetic field under analysis matched the geomagnetic field, and a bias magnetic field was generated using eight permanent magnets arranged in a Halbach configuration.[26,27]

The magnetic field measurements are represented in a 3D vector coordinate system. As the probe is reoriented, the resulting vectors trace trajectories on the surface of a sphere. The sphere's center corresponds to the bias magnetic field, which is considered static relative to the probe, whereas the sphere's radius equals the scalar magnitude of the geomagnetic field. Figure 3(b) illustrates a representative measurement outcome, where each data point denotes a discrete magnetic field reading. Each fitted circular trajectory corresponds to measurements acquired as the probe is discretely rotated within a single plane across a set of predefined angular orientations. A sphere is then fitted to all data points, and its center coordinates provide the calibrated bias field.

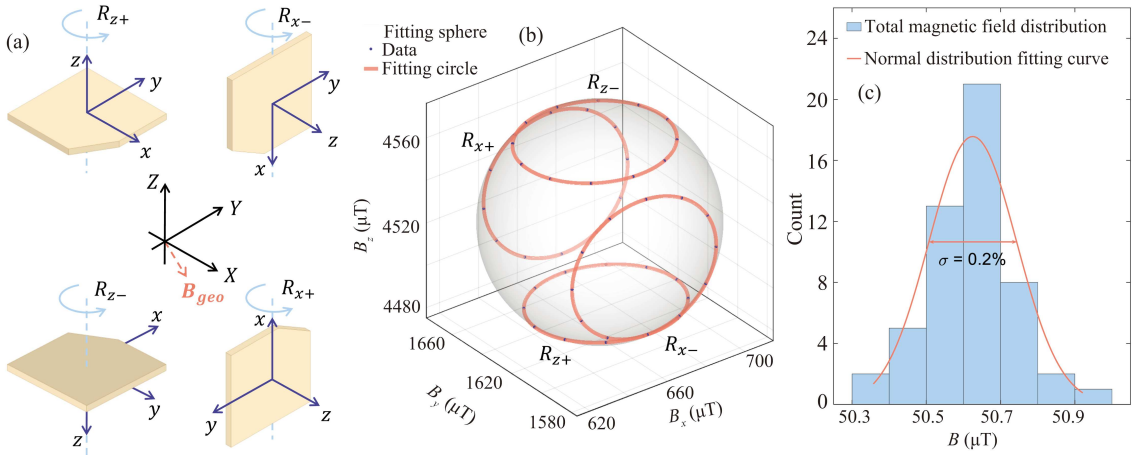


Fig. 3. Calibration method and the measurement results. (a) Schematic diagram of the experimental process. The probe is mounted on a turntable, which rotates along the spindle to perform magnetic field measurements at different orientations. Four sets of experiments are performed, with the turntable spindle aligned parallel to either the z- or x-axis of the diamond coordinate system. (b) Spherical fitting in vector space. For each experimental set (see panel (a)), the turntable rotates the probe within a single plane. The measurement data points are used to fit four red circles accordingly. A sphere (gray) is fitted to the complete dataset, where its center represents the bias field vector and its radius equals the magnitude of the environmental field. (c) Distribution of the measured total geomagnetic field. All test results are fitted to a normal distribution curve (red curve). The standard deviation of the fitted distribution is 0.1 μT.

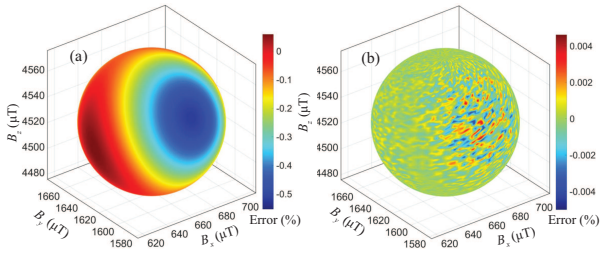


Fig. 4. The simulated errors of the total field measurements under a 50-μT geomagnetic field. The spin–strain coupling parameters are set to $M_x = \{2.9, 1.7, 2.0, 3.3\}$ MHz, $M_y = \{2.1, 2.2, 1.6, 1.6\}$ MHz, $M_z = \{4.0, 5.4, 6.0, 4.7\}$ MHz based on the measured stress tensor.[32,33] The bias magnetic field is fixed at $(664, 1627, 4526)$ μT. (a) Error distribution due to uncalibrated spin-strain coupling. Each point on the sphere represents a vector measurement at a distinct probe orientation. The color mapping on the sphere surface indicates the relative error in the measured geomagnetic field magnitude. The simulation yields a standard deviation of 0.07 μT for the total geomagnetic field. (b) Residual error after calibrating the spin–strain coupling parameters. Random perturbations within the reported uncertainty ranges of the stress tensor components are introduced (*e.g.*, $\sigma_{xx} \leq 5$ MPa and $\sigma_{zz} \leq 2$ MPa). The maximum relative error remains below 0.01% of the total geomagnetic field.

The total magnetic field measurement result for each observation is expressed as

$$|\boldsymbol{B}|^2 = (B_x - c_x)^2 + (B_y - c_y)^2 + (B_z - c_z)^2, \tag{2}$$

where $\boldsymbol{B}$ represents the target total magnetic field, (B_x, B_y, B_z) are the measured magnetic field vector components of $\boldsymbol{B_0}$, and (c_x, c_y, c_z) denotes the coordinates of the fitting sphere's center in vector space.

As illustrated in Fig. 3(c), the geomagnetic field measurements follow a normal distribution, as anticipated. The fitted distribution yields a central value of 50.6 μT and a standard deviation of 0.1 μT, corresponding to 0.2% of the total geomagnetic field. The maximum observed deviation is 0.3 μT. These deviations originate from several factors. The primary source is the fluctuation of the bias magnetic field, which exhibits a temperature dependence of −0.85 μT/K. Additional contributing factors include magnetic interference from the turntable and spatial inhomogeneity of the environmental magnetic field (see Appendix A).

To improve measurement accuracy, the spin–strain coupling parameters $(M^i_{x_i}, M^i_{y_i}, M^i_{z_i})$ should be determined by measuring the stress tensor inside the diamond sample.[31,32] For the present error analysis, we adopt the experimentally measured stress tensor values from Ref. [33] as follows:

$$\overleftrightarrow{\sigma} = \begin{pmatrix} 290(5) & 90(0) & 6(0) \\ 90(0) & 758(0) & 45(0) \\ 6(0) & 45(0) & -14(2) \end{pmatrix} \text{MPa}. \tag{3}$$

Simulations show that neglecting the spin–strain coupling introduces a standard deviation of 0.07 μT in the total geomagnetic field measurements, as depicted in Fig. 4(a). Assuming prior calibration of the stress tensor as described above, random perturbations within the reported uncertainty range are introduced to model variability.

As shown in Fig. 4(b), the resulting error of the total geomagnetic field remains below 0.01% after such calibration.

4. Conclusion

In this study, the vector magnetic field is inferred from the resonance frequencies of NV center ensembles based on the system Hamiltonian. A bias field calibration method is introduced, in which the probe is reoriented to measure vector-total magnetic fields in multiple orientations. This method serves both to calibrate the bias magnetic field and to independently verify the accuracy of the total magnetic field measurements. The precision is primarily constrained by fluctuations in ambient temperature and the magnetic perturbation from the testing equipment. Future implementations could benefit from integrating a temperature control device to minimize fluctuations in the bias magnetic field and from calibrating the stress tensor. These enhancements are expected to suppress environmental

noise and Hamiltonian-related errors, thereby improving measurement fidelity and potentially achieving an accuracy better than 0.01%.

Magnetic sensing techniques based on NV center ensembles have emerged as pivotal tools in advanced research, including magnetic field imaging,[34–36] bio-sensing,[37–39] and condensed matter characterization.[40,41] Recently, compact integrated magnetometers based on NV centers have been applied in scenarios beyond the laboratory.[42] In 2021, a quantum diamond-based magnetometer known as OSCAR–QUBE was installed aboard the International Space Station, where it successfully generated geomagnetic maps throughout its operational lifespan.[43] In the future, this magnetometry has the potential for effective deployment across various applications.

Owing to the rigid crystallographic structure of diamond, NV center ensembles are capable of measuring both the vector magnetic field and its total magnitude. The bias field calibration method introduced in this study corrects zero-offset errors without relying on auxiliary magnetometers, offering a clear advantage over conventional vector fluxgate sensors. With its remarkable sensitivity and suitability for compact system integration, the NV center-based magnetometry emerges as an optimal choice for spacecraft instrumentation. This technique enables meaningful reductions in payload mass and operational costs, while contributing to extended mission durations.

Appendix A: Environmental perturbations

The accuracy of the total magnetic field measurements is affected by environmental perturbations, including temperature fluctuations, magnetic interference from the turntable, and spatial inhomogeneity of the ambient field. Temperature fluctuations predominantly alter the bias magnetic field. To characterize this effect, total magnetic fields were measured using the NV probe under varying environmental temperatures. The results indicate a linear dependence with a coefficient of −0.85 μT/K, as shown in Fig. A1(a).

The magnetic interference from the turntable was characterized by placing an atomic magnetometer at its center to record the magnetic field during rotation. The maximum disturbance observed was 0.06 μT, as illustrated in the following Fig. A1(b).

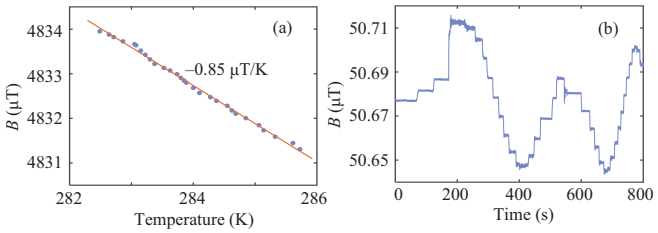


Fig. A1. Disturbances in total magnetic field measurements under different conditions. (a) Temperature dependence. The total magnetic field is recorded by the NV probe as a function of ambient temperature, which is simultaneously measured by a thermometer. A linear fit reveals that the bias magnetic field varies at a rate of approximately −0.85 μT/K. (b) Magnetic interference from the turntable. An atomic magnetometer continuously measures the total magnetic field while the turntable rotates in 20° increments, with a pause at each position. The maximum magnetic disturbance observed during rotation is 0.06 μT.

Appendix B: Magnetometers comparison

A comparative overview of this work and other magnetometers deployed on spacecraft is presented in Table B1. While fluxgate magnetometers are the most prevalent technology in space applications, the present setup demonstrates better performance in total field reconstruction compared to uncalibrated fluxgate devices.[44]

To date, the OSCAR–QUBE remains the only NV center magnetometer operated on a spacecraft.[43] The setup presented in this work exhibits enhanced sensitivity, albeit at the cost of increased power consumption. With further optimization, this technology is suitable for vector–total magnetic field measurements in future space missions.

Table B1. Magnetometers on spacecraft[7,43] compared with this work. FGM: fluxgate magnetometer; SHM: scalar helium magnetometer; B: biaxial; T: triaxial; S: scalar; *: using sensitivity.

Mission	Launch year	Magnetometer	Dynamic range (nT)	Resolution (pT)	Mass (kg)	Power (W)
GOES-1-3	1975–1978	FGM (B)	50–400	–	–	–
GOES-4-7	1980–1987	FGM (B)	±400	200	–	–
GOES-I-M	1994–2001	FGM (T)	±1000	100	–	–
Cassini	1997	FGM (T)	±40	4.9	0.44	7.5 (sleep)
		SHM (S)	±10000	1200	0.71	12.63 (FGM + SHM)
GOES-N-P	2006–2010	FGM (T)	±512	30	–	–
Juno	2011	FGM (T)	±1600 (nominal)	48	5	> 4.5
			±1638400 (max.)	5000	–	–
MAVEN	2013	FGM (T)	±512	15	–	> 1
			±2048	62	–	–
GOES-R	2016	FGM (T)	±512	16	2.5	4
OSCAR-QUBE	2021–2022	NV (T)	±1860000	300000*	0.42	5
This work	–	NV (T/S)	±1000000	2500*	0.5	50

Acknowledgment

Project supported by the Key Research and Development Program of Zhejiang Province, China (Grant No. 2024SSYS0090), the Natural Science Foundation of Zhejiang Province, China (Grant No. LDQ24A040001), Dreams Foundation of Jianghuai Advance Technology Center (Grant No. 2023-ZM01X020), the National Key Research and Development Program of China (Grant No. 2023YFB3209900), the National Natural Science Foundation of China (Grant No. T2388102), "Pioneer" and "Leading Goose" Research and Development Program of Zhejiang Province, China (Grant No. 2025C01040), the Fundamental Research Funds for the Central Universities (Grant Nos. 226-2024-00144 and 226-2024-00011), the Postdoctoral Fellowship Program of CPSF (Grant No. GZC20252264), and the China Postdoctoral Science Foundation (Grant No. 2025M773438).

References

[1] Carletta S, Teofilatto P and Farissi M S 2020 *Aerospace* **7** 3
[2] Psiaki M L, Huang L and Fox S M 1993 *Journal of Guidance, Control, and Dynamics* **16** 206
[3] Wiegand M 1996 *Acta Astronautica* **38** 395
[4] Stolle C, Lühr H, Rother M and Balasis G 2006 *Journal of Geophysical Research: Space Physics* **111**
[5] Acuna M H 2002 *Rev. Sci. Instrum.* **73** 3717
[6] Primdahl F 1979 *J. Phys. E* **12** 241
[7] Bennett J S, Vyhnalek B E, Greenall H, Bridge E M, Gotardo F, Forstner S, Harris G I, Miranda F A and Bowen W P 2021 *Sensors* **21** 5568
[8] Schiffler M, Queitsch M, Stolz R, Chwala A, Krech W, Meyer H G and Kukowski N 2014 *Geophysical Journal International* **198** 954
[9] Kominis I K, Kornack T W, Allred J C and Romalis M V 2003 *Nature* **422** 596
[10] Budker D and Romalis M 2007 *Nat. Phys.* **3** 227
[11] Olsen N, Clausen L T, Sabaka T J, Brauer P, Merayo J M, Jørgensen J L, Léger J M, Nielsen O V, Primdahl F and Risbo T 2003 *Earth, Planets and Space* **55** 11
[12] Merayo J M, Brauer P, Primdahl F, Petersen J R and Nielsen O V 2000 *Measurement Science and Technology* **11** 120
[13] Shonibare T, Murphy K and Pakhotin I 2024 *Journal of Geophysical Research: Space Physics* **129** e2024JA032728
[14] Schloss J M, Barry J F, Turner M J and Walsworth R L 2018 *Phys. Rev. Appl.* **10** 034044
[15] Herbschleb E, Kato H, Maruyama Y, Danjo T, Makino T, Yamasaki S, Ohki I, Hayashi K, Morishita H, Fujiwara M, *et al.* 2019 *Nat. Commun.* **10** 3766
[16] Hong S, Grinolds M S, Pham L M, Le Sage D, Luan L, Walsworth R L and Yacoby A 2013 *MRS Bulletin* **38** 155
[17] Schirhagl R, Chang K, Loretz M and Degen C L 2014 *Annu. Rev. Phys. Chem.* **65** 83
[18] Kim D, Ibrahim M I, Foy C, Trusheim M E, Han R and Englund D R 2019 *Nat. Electron.* **2** 284
[19] Grotz B, Hauf M V, Dankerl M, Naydenov B, Pezzagna S, Meijer J, Jelezko F, Wrachtrup J, Stutzmann M, Reinhard F, *et al.* 2012 *Nat. Commun.* **3** 729
[20] Crawford S E, Shugayev R A, Paudel H P, Lu P, Syamlal M, Ohodnicki P R, Chorpening B, Gentry R and Duan Y 2021 *Adv. Quantum Technol.* **4** 2100049
[21] Barry J F, Schloss J M, Bauch E, Turner M J, Hart C A, Pham L M and Walsworth R L 2020 *Rev. Mod. Phys.* **92** 015004
[22] Felton S, Edmonds A, Newton M E, Martineau P, Fisher D, Twitchen D and Baker J 2009 *Phys. Rev. B* **79** 075203
[23] Goldman M L, Sipahigil A, Doherty M, Yao N Y, Bennett S, Markham M, Twitchen D, Manson N, Kubanek A and Lukin M D 2015 *Phys. Rev. Lett.* **114** 145502
[24] Goldman M L, Doherty M, Sipahigil A, Yao N Y, Bennett S, Manson N, Kubanek A and Lukin M D 2015 *Phys. Rev. B* **91** 165201
[25] Tamarat P, Manson N, Harrison J, McMurtrie R, Nizovtsev A, Santori C, Beausoleil R, Neumann P, Gaebel T, Jelezko F, *et al.* 2008 *New J. Phys.* **10** 045004
[26] Yu Z, Zhu Y, Zhang W, Jing K, Wang S, Chen C, Xie Y, Rong X and Du J 2025 *National Science Review* nwae478
[27] Zhu Y, Wang K, Yu Z, Qiu Y, Qiao Y, Wang S, Jing K, Xie Y and Rong X 2025 *Diamond and Related Materials* 112521
[28] Le Sage D, Pham L M, Bar-Gill N, Belthangady C, Lukin M D, Yacoby A and Walsworth R L 2012 *Phys. Rev. B* **85** 121202
[29] Alegre T P M, Santori C, Medeiros-Ribeiro G and Beausoleil R G 2007 *Phys. Rev. B* **76** 165205
[30] Shin C S, Avalos C E, Butler M C, Trease D R, Seltzer S J, Peter Mustonen J, Kennedy D J, Acosta V M, Budker D, Pines A, *et al.* 2012 *J. Appl. Phys.* **112**
[31] Doherty M, Dolde F, Fedder H, Jelezko F, Wrachtrup J, Manson N and Hollenberg L 2012 *Phys. Rev. B* **85** 205203
[32] Broadway D A, Johnson B, Barson M, Lillie S E, Dontschuk N, McCloskey D, Tsai A, Teraji T, Simpson D, Stacey A, *et al.* 2019 *Nano Lett.* **19** 4543
[33] Grazioso F, Patton B R, Delaney P, Markham M L, Twitchen D J and Smith J M 2013 *Appl. Phys. Lett.* **103**
[34] Arai K, Belthangady C, Zhang H, Bar-Gill N, DeVience S, Cappellaro P, Yacoby A and Walsworth R L 2015 *Nat. Nanotechnol.* **10** 859
[35] Pham L M, Le Sage D, Stanwix P L, Yeung T K, Glenn D, Trifonov A, Cappellaro P, Hemmer P R, Lukin M D, Park H, *et al.* 2011 *New J. Phys.* **13** 045021
[36] Maertz B, Wijnheijmer A, Fuchs G, Nowakowski M and Awschalom D 2010 *Appl. Phys. Lett.* **96** 092504
[37] Le Sage D, Arai K, Glenn D R, DeVience S J, Pham L M, Rahn-Lee L, Lukin M D, Yacoby A, Komeili A and Walsworth R L 2013 *Nature* **496** 486
[38] Balasubramanian G, Chan I, Kolesov R, Al-Hmoud M, Tisler J, Shin C, Kim C, Wojcik A, Hemmer P R, Krueger A, *et al.* 2008 *Nature* **455** 648
[39] Zhang T, Pramanik G, Zhang K, Gulka M, Wang L, Jing J, Xu F, Li Z, Wei Q, Cigler P, *et al.* 2021 *ACS Sensors* **6** 2077
[40] Xu Y, Zhang W and Tian C 2023 *Photonics Research* **11** 393
[41] Casola F, Van Der Sar T and Yacoby A 2018 *Nat. Rev. Mater.* **3** 1
[42] Webb J L, Clement J D, Troise L, Ahmadi S, Johansen G J, Huck A and Andersen U L 2019 *Appl. Phys. Lett.* **114** 231103
[43] Beerden Y, Vandebosch R, Ermakova A, Nesladek M and Hruby J 2024 *IEEE International Geoscience and Remote Sensing Symposium* (IEEE) pp. 465–468
[44] Xu C, Huang K, Zhang S and Meng L 2020 *IOP Conference Series: Earth and Environmental Science* Vol. 446 (IOP Publishing) p. 052087